www.elsevier.com/locate/ijadhadh

Numerical design and multi-objective optimisation of novel adhesively bonded joints employing interlocking surface morphology

M.C. Corbett, P.A. Sharos, M. Hardiman, C.T. McCarthy

PII: S0143-7496(17)30104-5
DOI: http://dx.doi.org/10.1016/j.ijadhadh.2017.06.002
Reference: JAAD2015

To appear in: *International Journal of Adhesion and Adhesives*
Accepted date: 12 June 2017

Cite this article as: M.C. Corbett, P.A. Sharos, M. Hardiman and C.T. McCarthy Numerical design and multi-objective optimisation of novel adhesively bonde joints employing interlocking surface morphology, *International Journal o Adhesion and Adhesives,* http://dx.doi.org/10.1016/j.ijadhadh.2017.06.002

Numerical design and multi-objective optimisation of novel adhesively bonded joints employing interlocking surface morphology

M.C. Corbett[a], P.A. Sharos[a], M. Hardiman[a], C.T. McCarthy[a,*]

[a] *Bernal Institute, School of Engineering, University of Limerick, Limerick, Ireland*

Abstract

A novel concept for joining materials is presented which employs adhesive joints with interlocking bond-surface morphology formed on the surfaces of male and female adherends which mechanically interlock in shear when brought together. In the present work, miniature, single-lap joint specimens with a single truncated square pyramid interlocking profile, centred in the bond area, are investigated. The performance of the concept is assessed through finite element analysis (FEA) by incorporating yield criteria representing plasticity in the adherends and a cohesive zone model to represent damage in the adhesive layer. This allows for effective simulation of the joint response until ultimate failure and thus, full assessment of the concept's performance. Various interlocking geometries are explored and refined through an adaptive surrogate modelling design optimisation procedure coupled with FEA. The results indicated that significant improvements in work to failure, of up to 86.5%, can be achieved through the more progressive failure behaviour observed compared to that of a traditional adhesively bonded joint. Improvements in the joint's ultimate failure load can also be achieved with a relatively ductile adhesive system.

Keywords: finite element stress analysis; cohesive zone model; adhesion by mechanical interlocking; hybrid joints; joint optimisation

1. Introduction

Joining is a critical element of engineering design. It provides the ability to achieve structural size and shape complexity which is beyond the capabilities of primary manufacturing processes; allows for optimal material selection and usage; provides impact and damage tolerance beyond that inherent in the materials of construction; and facilitates disassembly for repair or responsible disposal of components. Each of these features directly influence the cost of a structure, which is a key driver in any engineering design. However, joining also represents one of the greatest challenges in the design of structures in general, as the strength of a joint dictates the strength and efficiency of the surrounding structure.

There are three fundamental processes by which materials and structures can be joined: (1) mech-

*Corresponding author: Tel.:+353 (0)61234334; Fax: +353 (0)61202944
Email address: conor.mccarthy@ul.ie (C.T. McCarthy)

anical fastening, (2) chemical bonding, and (3) thermal joining. In consideration of structural applications, bolting, adhesion and welding are the primary techniques of choice. Individually, these technologies present inherent weaknesses which are outlined through the abundance of publications on each. Bolted joints are reliable but result in inefficient connections which reduce the strength of parent materials by introducing a stress concentration; and also add weight to the structure. Adhesive bonding provides greater efficiency but its uptake in load-bearing structures has been slow, due primarily to unpredictable joint strengths caused by variability in surface preparation techniques, which can lead to certification issues [1]. Safety considerations often require that adhesively bonded structures, particularly those employed in primary load-bearing applications, include mechanical fasteners as an additional precaution [2, 3]. These practices result in heavier and more costly components. Welded joints present difficulty when joining dissimilar materials and often have lower structural stiffness than equivalent adhesively bonded joints.

The aforementioned techniques have undergone significant development in the past number of decades in order to approach the pinnacle of their potential performance. More recently, a number of hybrid methods, which combine the positive traits of the fundamental processes, have been developed in literature. Mechanical/thermal-adhesive joining techniques, such as bonded/bolted and weld/bonded joints, have been considered in relation to improving damage tolerance of adhesive joints [4–10]. The Welding Institute has also developed an entirely novel technique for joining composites to metals [11]. Given the significant developments in materials science and manufacturing technology, there is a momentous opportunity for the development of new hybrid joining processes which may leverage the evolution of joining technology in the 21^{st} century.

The present work focusses on the development of a novel, hybrid mechanical-adhesive joining technology. The central bond region of a traditional adhesively bonded joint is widely recognised as being relatively inactive for load transfer and during joint failure. Rather, load is predominantly transferred through the overlap ends and failure is typically a direct function of the stress state in these regions, where the highest strains occur and normal and tangential stresses localise in the adhesive layer. As a result, fracture typically initiates in the adhesive at the free ends of the joint overlap, leading to sudden and catastrophic failure. Some authors have even shown that removing the adhesive in the central overlap region of the joint causes minimal effect to the adhesive stress state, i.e. recessed adhesive joints [12]. Previous authors have shown that modifications of the bond surface topology can alter the stress state in the adhesive bond line, culminating in compelling improvements in both

ultimate failure load and damage tolerance of adhesive joints [13, 14]. In order to activate the central bond region of the joint, the concept under consideration employs interlocking profiles, formed on the surfaces of male and female adherends, coupled with a layer of adhesive. The interlocking surfaces could serve to increase mechanical loading within the joint akin to mechanically fastening and thus improve reliability. They should also distribute load more evenly across the lap area and delay crack propagation through the adhesive; thereby overcoming some of the major weaknesses of traditional adhesive joints.

Herein, the joining concept is investigated through finite element (FE) analysis for a miniature adhesive joint with a single, interlocking profile in the centre of its bond area. A cohesive zone damage model (CZDM) is used to simulate damage in the adhesive and capture the response of the joint until catastrophic failure. Various profile geometries have been investigated in order to develop a fundamental understanding of the underlying mechanics of the interlocking joint and assess the performance of the concept. In order to efficiently explore the design space and determine the most effective interlocking geometry, an adaptive surrogate modelling design optimisation (ASMDO) methodology is employed. A multi-objective evolutionary optimisation algorithm is subsequently applied directly to the surrogate model to fully outline the performance envelope of the concept through a Pareto optimal design front.

2. Methodology

2.1. Joint Geometry

The test specimen geometry was chosen, conductive to associated experimental work, as an adhesively bonded miniature single-lap joint (SLJ), shown in Figure 1a. This specimen was similarly adopted by O'Dwyer et al. [15] and allows for in situ testing within an SEM chamber. In order to simplify the FE mesh, no adhesive fillet was included in the model geometry. A single truncated square pyramid surface profile, centred in the 35mm^2 bond area, was investigated. This morphology represented the most fundamental interlocking design, allowing for its influence on joint performance to be effectively investigated. The surface profile was parametrised into four factors; length (X_1), depth (X_2), width (X_3), and inclination angle (X_4) (Figure 1b), so that its design may be subsequently optimised. Thus, the interlocking joint consisted of a female adherend, with a depression in its surface and a male adherend, with a protruding profile defined to fit the female adherend. The adherends were coupled with a constant thickness adhesive layer, of 55 μm [15], between the interlocking surfaces (see Figure 1a).

2.2. Finite Element Model

Implicit simulations were conducted with Abaqus® [16]. The test specimen was loaded in quasi-static, displacement controlled tension from the grip locations shown in Figure 1a. The adherends were simulated as an aluminium alloy, AA5754 [17]. The stress-strain response of the alloy was sourced from literature [18], salient mechanical properties are summarised in Table 1. The response of the alloy was characterised by elastic-plastic behaviour incorporating von Mises yield criteria. Post-yield response was represented by isotropic strain hardening defined through Holloman's equation [19] (Eq. 1). This material was represented by 8-node, linear, brick elements with reduced integration and hourglass control (C3D8R) [16]. No damage model was implemented in the adherends as cohesive failure of the joint was assumed.

$$\sigma = K\varepsilon_p^n \tag{1}$$

where σ is the true stress, K is the strength coefficient, ε_p is the true plastic strain and n is the strain hardening exponent.

The adhesive adopted in this investigation was a bi-component structural epoxy resin, Loctite® Hysol 9466 [20]; its bulk mechanical properties were characterised comprehensively by Goglio et al. [21] and are summarised in Table 2. A cohesive zone damage model (CZDM) was implemented in consideration of damage within the adhesive layer. The CZDM chosen is implemented in Abaqus® 6.14 [16]. It is a coupled mixed-mode CZDM and thus accounts for interaction between both normal (mode I) and tangential (mode II & III) deformation of the adhesive layer. In the FE mesh, the adhesive layer was represented with its true thickness by a single layer of 8-node cohesive elements (COH3D8). In each mode the response of these elements obeyed a bi-linear traction-separation law with linear softening. This response has been shown to approximate the true mechanical behaviour of a constrained adhesive layer in pure mode I [22] and pure mode II [23], as demonstrated by Högberg [24].

The initial stiffness of the cohesive elements is governed by a penalty parameter, k, determined according to the Abaqus® user's manual [16]. Interaction between each mode of loading for the initiation of damage was accounted for according to the quadratic stress criterion, as per Eq. 2. This rule has previously achieved excellent agreement to experimental tests of adhesive joints [25, 26].

$$\left(\frac{\langle t_n \rangle}{t_n^o}\right)^2 + \left(\frac{t_s}{t_s^o}\right)^2 + \left(\frac{t_t}{t_t^o}\right)^2 = 1 \tag{2}$$

where t_n, t_s and t_t represent the normal, in-plane tangential and out-of-plane tangential tractions respectively, and t_n^o, t_s^o and t_t^o are the critical traction values in each mode.

Once damage is initiated, the stiffness of the cohesive elements softens progressively according to a damage parameter, D, which monotonically evolves from 0 to 1 upon further loading after damage initiation. Damage evolution was controlled by the linear fracture energetic criterion according to Eq. 3, as similarly applied to adhesive joints by numerous authors [26]. Once this criterion is satisfied D is set to 1, the element may no longer carry load and is deleted from the model thus allowing fracture to propagate.

$$\left(\frac{G_n}{G_n^C}\right)^\alpha + \left(\frac{G_s}{G_s^C}\right)^\alpha + \left(\frac{G_t}{G_t^C}\right)^\alpha = 1 \tag{3}$$

where G_n, G_s and G_t represent the normal, in-plane tangential and out-of-plane tangential fracture energy release rates respectively, G_n^C, G_s^C and G_t^C are the critical fracture energies in each mode, and $\alpha = 1$ for the linear fracture energetic criterion.

The properties of the CZDM were chosen to be equal for both normal and tangential loading, to those retrieved experimentally by Pirondi et al. [25] using pure mode I, double-cantilever beam tests. This approximation is partially justified by the brittle behaviour this adhesive exhibits in traction [21]. A similar modelling approach was successfully adopted by Castagnetti et al. [27] for the same adhesive and similar bond thickness; showing strong correlation to experiments.

2.3. Surrogate Modelling & Optimisation

In order to conduct a broad exploration of the design space and exploit the maximum potential from the concept, an adaptive surrogate modelling methodology was employed [28]. The surrogate model approximates the results of the computation-intensive finite element joint simulations with simple computationally efficient analytical models. In this way, it is possible to construct a comprehensive view of the concept's performance across the entire design space based on a finite number of computationally expensive simulations. This capability provides vital decision support to various design considerations, as the surrogate model can be employed instantly to study the sensitivity and effect of the interlocking surface design factors on the joint's performance. In addition, sophisticated optimisation algorithms

may be applied to directly search the surrogate model, thereby making it feasible to carry out global multi-objective optimisation of the joint's performance.

The steps of the adaptive surrogate modelling design optimisation (ASMDO) process, as applied to the present investigation, are outlined in Figure 2. Initially, the problem is formulated such that input factors and output responses are designated for the given problem (see Section 2.3.1). The initial design of experiment (DOE) is outlined to designate the input factors which dictate the design of the interlocking surfaces in each simulation. An optimal Latin hypercube was employed herein, which guarantees space-filling of the design space and is recommended for computer experiments [29]. Next, finite element simulations are conducted (as outlined in Section 2.2) to determine the performance of each interlocking design outlined in the DOE. The surrogate model (approximation) is then constructed based on these simulation results to estimate the interlocking concept's performance across the entire design space. Kriging was employed in this case; the mathematical formulation of which can be found in Forrester et al. [29]. Additional simulations may be added sequentially at this point, until satisfied with the model accuracy prior to optimisation. The design of the interlocking surfaces is subsequently optimised based on the surrogate model. The approximation may be further refined in regions of interest by conducting additional simulations until satisfied with the results or the computational budget is met.

In the case that the surrogate model accuracy is insufficient or an optimum design is not located based on the initial DOE, it is prudent to enhance the model by adding infill points (i.e. additional FE simulations). The choice of infill point is critical, one may choose to locally exploit the model, to enhance its accuracy in a recognised, optimal region, or globally explore the model, to augment its overall accuracy. A review of various adaptive sampling techniques was conducted in [30]. The technique selected herein balances a combination of local exploitation and global exploration through a multi-objective algorithm which maximises the expected improvement of an infill point in terms of both objective functions; as formulated by Forrester et al. [29].

2.3.1. Optimisation Problem

The design vector, $\mathbf{X}$ containing the factors for each simulation (see Figure 1b) is presented per Eq. 4. In order to define the design space, side constraints were placed on each design factor, as outlined in Table 3. These constraints were based on the joint geometry as well as practical manufacturing constraints. It was also necessary to impose inequality constraints in order to ensure the interlocking geometry was non-intersecting. These constraints were specified as per Eq. 5 and Eq. 6 in the x- and

z-directions respectively. In order to facilitate machining, a minimum width of $0.55mm$ (corresponding to the tool width) was enforced at the narrowest cross section of the interlocking profile.

$$\mathbf{X} = [X_1, X_2, X_3, X_4] \tag{4}$$

$$g_1(\mathbf{X}) = \frac{X_1}{2} - \frac{X_2}{\tan(X_4)} - 0.55 \tag{5}$$

$$g_2(\mathbf{X}) = \frac{X_3}{2} - \frac{X_2}{\tan(X_4)} - 0.55 \tag{6}$$

The performance of the concept was based on two joint performance indicators, ultimate failure load (maximum force sustained by the joint), y_1, and work to failure, which is the work required to break the joint (the area beneath the load-displacement curve), y_2. It should be noted that the energy absorbed by the joint in the early stages of loading is mainly due to elastic deformation, and is recovered when the specimen is unloaded. The non-dominated sorting genetic algorithm (NSGA-II) [31] was applied to the surrogate model in order to address the compromise between these objectives and establish Pareto-optimal design solutions. The multi-objective optimisation problem is formulated as follows:

$$\begin{aligned} &\text{Maximise} && f_i(\mathbf{X}) = \bar{y}_i, \quad i = 1, 2 \\ &\text{subject to} && g_j(\mathbf{X}) > 0, \quad j = 1, 2 \end{aligned} \tag{7}$$

where $\bar{y}$ is the output from the surrogate model, $i, j = 1$ represents the ultimate failure load objective function, and $i, j = 2$ represents the work to failure objective function.

3. Numerical Validation

3.1. Mesh Independence

Model creation and meshing were automated through a Python™ script. Global and local nodal seeds were appropriately assigned such that seed density was increased at the ends of the joint overlap and in the vicinity of the interlocking profile; with the overall base seed size controlled by a variable in the Python™ script. An interlocking joint model was generated with profile length, depth, width,

and angle of $1.84mm$, $1.0mm$, $5.9mm$, and $80.0°$ respectively. The base mesh size was varied to generate ten FE models with total degrees of freedom (DOF) ranging from 30.2×10^3 to 1.4×10^6 (836 to 12,504 cohesive elements). The ultimate failure load and the ultimate displacement at failure of each simulation were monitored in order to determine convergence of the results and thus, the most computationally efficient mesh. The results are presented in Figure 3. The selected, most efficient, model discretisation is indicated by an arrow; with 5.14×10^5 DOF and 5,936 cohesive elements. The size of the smallest and the largest cohesive elements in this model were $35.9 \times 55 \times 71.4\mu m$ and $82.5 \times 95.35 \times 55\mu m$, respectively. These element sizes ensured that during fracture propagation the process zone encompassed at least 4 to 5 elements in all simulations. This ensured that cohesive tractions at the crack tip were accurately resolved and also prevented numerical instability [32, 33].

3.2. Surrogate Model Verification

The accuracy of the surrogate models were verified through a *leave-one-out* cross-validation procedure [34]. During this process, the results from one finite element simulation were removed. The remaining simulations were used to re-construct the surrogate models which were subsequently used to predict the results of the omitted simulation. The differences between the predictions and the actual results were compared and this procedure was repeated for each simulation conducted in order to quantify the prediction errors across the design space. The primary results of this procedure are illustrated per Figure 4. The correlation coefficients, R^2 for the ultimate failure load and the work to failure surrogate models were 0.986 and 0.846 respectively.

4. Results & Discussion

4.1. Design Exploration & Optimisation

In total, thirty FE simulations were engaged by the ASMDO process, eight deriving from the initial DOE and twenty-two generated through the adaptive sampling and optimisation process. A selection of interlocking designs, labelled A through N, have been chosen to demonstrate the characteristics of the concept; their respective design properties and performance are outlined in Table 4. Dependent on the interlocking geometry, each joint produced unique mechanical response. Examples of this behaviour are given in Figure 5, in which the load-displacement response of various interlocking joints are compared to that of a standard adhesively bonded joint modelled with equivalent properties, referred to as the baseline joint. The diversity in the response of each joint culminated in different

values of the objective functions, ultimate failure load and work to failure. In order to determine the influence of the profile geometry on the objective functions, design of experiments and regression analysis techniques were employed to definitively evaluate the factor effects. A full factorial experiment with six levels was conducted, resulting in a requirement for 1,296 simulations. In place of these simulations, the response was determined directly from the surrogate models, based on the thirty simulations previously conducted. The main effects for each factor were determined by fitting the results of the full factorial experiment to a quadratic polynomial. In this way it was possible to determine the *linear* and *quadratic main* effects of each factor; as well as two-way interaction effects. In this section, only the most significant factor effects are discussed, i.e. those with normalised effect relative to one another of greater than 5%.

The main effects corresponding to the ultimate failure load response are shown in Figure 6a. Profile length (X_1), has the most significant effect. Increasing profile length decreases the ultimate failure load (negative effect). The effect of profile length also presents significant negative non-linearity, indicating that there is a threshold below which profile length does not have a meaningful influence. Analysis of the surrogate model revealed that profiles with length less than approximately 50% of the bond length (x-direction) produced a reduction in ultimate failure load of less than 5% compared to the baseline. Profile depth (X_2) and width (X_3) also have strong negative linear effects and there is substantial negative synergistic interactions between profile length and depth (X_1 & X_2), as well as profile length and width (X_1 & X_3) (Figure 6b). For low values of profile depth (X_2), the influence of profile length (X_1) is less, and visa versa; similar interaction is present between profile length and width (X_1 & X_3). Profile depth and width (X_2 & X_3) also present less considerable interaction. Profile inclination angle (X_4) appears to have a negligible effect on ultimate failure load.

The main effects corresponding to the work to failure response are shown in Figure 6c. Profile width (X_3) presents the greatest *linear main* effect, followed by profile angle (X_4), and profile depth (X_2). The work to failure increases as each these variables are increased (positive effect). Positive synergistic interaction between profile width and angle (X_3 & X_4) has the most significant effect overall, while important interactions also exist between profile depth and width (X_2 & X_3), and profile depth and angle (X_2 & X_4) (Figure 6d). These interactions indicate that given a low value of any one of these factors (X_2, X_3 or X_4), the effect of the other two factors becomes much less meaningful. Profile width and angle (X_3 & X_4) also present significant positive non-linearity, indicating that the greatest improvements in work to failure are only achieved for high values of these factors. Profile length (X_1)

appears to have an insignificant effect on work to failure.

Analysis of the factor effects affirms the requirement for multi-objective optimisation; as a conflict exists between the objectives, principally depending on profile depth and width. A Pareto optimal set of 10 designs was established from the thirty simulations conducted. Each of these designs were optimal such that, no one design presented performance which was better than any other design in terms of both objectives. The performance of each of these simulations is presented in the Pareto plot in Figure 7. Also shown is the Pareto frontier, identified by the optimisation algorithm based on the surrogate models, indicating the accuracy of the surrogate models in optimal regions of the design space; it important to note the range of the plot axes when considering this accuracy. Importantly, the Pareto frontier indicates the bounds of performance which may be achieved for the concept and the present material systems. It is clear that considerable improvements may be achieved in work to failure, of up to 86.5%. Improvements in ultimate failure load were less significant, although optimal configurations demonstrate minimum reduction compared to the baseline.

In consideration of the magnitude of performance improvement identified in comparison to the baseline and noting the range of the of responses achieved amongst the Pareto optimal design set, it was clear that improvements in terms of work to failure were much more significant than that of ultimate failure load. Thus, joint N was selected as the optimum design. It exhibited the greatest improvement in work to failure (86.5%) with only 1.2% reduction in ultimate failure load (based on FE simulation). The mechanical response of this joint will be discussed in the ensuing sections.

4.2. Linear Elastic Analysis

The stress distribution in the adhesive layer prior to damage initiation was investigated by modelling the adhesive as a linear elastic material, as in Section 2.2, and applying a constant joint load of 300N. Three joint configurations were investigated: interlocking joints C and N, and the baseline joint. The stress distributions were extracted along a path at the centre of the adhesive thickness, on the joint's x-y mid-plane. The resulting normal and tangential stress distributions are presented in Figure 8. In order to discuss the influence of the interlocking morphology herein, the bond was described by its male end, i.e. the end of the bond closest to the constraint of the male adherend, and vice versa, its female end. The cutaway cross-sectional profiles of each adhesive layer are also provided above Figure 8 for clarity.

Initial examination of the stress distribution in the adhesive of the interlocking joints revealed similar concentrations of normal and tangential stress at the free ends of the joint overlap to that of

the baseline joint and typical to the SLJ. However, distinct differences between the interlocking and baseline configurations were also directly apparent. For example, in consideration of the tangential stress (in-plane, mode II), there was considerable asymmetry in the stress distribution between the male and female ends of the bond. The difference between the peak tangential stress was 34.3% and 13.2% for joints C and N respectively, with the maximum at the female end in each case. This phenomena may be explained through Volkersen's concept of differential shear [35]. Consider the cross-sectional drawings of the joint overlap illustrated in Figure 8, section Y-Z. The female adherend of the interlocking joint has a smaller cross-sectional area than that of the male adherend. Consequentially, there is greater tensile deformation of the female adherend in the vicinity of the profile. This results in lesser differential shear between the male and female adherends at the male end of the joint overlap and thus less tangential stress in the adhesive. Inversely, the tangential stress at the female end of the overlap is increased slightly.

Minimal tangential stress was transferred along the base of the interlocking profile and the average tangential stress was 45.2% and 37.6% less than the baseline for joints C and N respectively. Notably, sharp changes in stress were also evident at the edges of the interlocking profiles. These arose from the sudden change in orientation system in the region of high stress gradients where these irregularities occur. There was also negative tangential stress in the adhesive at the profile face at the male end of the overlap, while minimal tangential stress was observed at the profile face at the female end of the overlap.

In terms of normal stress, the interlocking joints correspond much more closely to the baseline. The maximum normal stresses at the ends of the overlap were 9.4% and 6.6% greater than the baseline for joints C and N respectively, occurring in both cases at the female end of the overlap. Asymmetry in the stress distribution was less pronounced than in the tangential stress distribution. The difference between the peak normal stress at the male and female ends of the bond was 6.8% and 10% for joints C and N respectively. This asymmetry may be explained by analogy to the analysis of Goland and Reissner [36] that deduced that a bending moment, M and a transverse force, V act indirectly on the SLJ as a result of the eccentricity of the applied forces (Figure 8). Assuming that the adhesive was relatively flexible compared to the adherends and deformation of the adherends was a result of tensile stress in the loading direction only, it was shown that bending of the adherends resulted in transverse normal stress through the thickness of the adhesive layer. In the case of the interlocking adhesive joint, there is increased bending of the female adherend as a result of the reduced second moment of area in

the vicinity of the interlocking profile. As a result, the normal stress in the adhesive at the female end of the overlap is increased.

It was also observed that the reduced second moment of area in the vicinity of the profile and the forces of adhesion on the bond-plane caused the extrusion in the female adherend to open, resulting in a "loose fit condition" for the interlocking joint, as illustrated in Figure 8. As a consequence, minimal load was transferred due to contact of the mechanical interlock. In fact, tensile normal stresses were observed on the faces of the interlocking profile because of this loose fit condition. The difference in the magnitudes of the stresses on the profiles faces at the male and female ends of the bond were due to the geometry and loading direction, as a small amount of load was transferred back through the profile face at the male end of the bond. The relative inactivity of the mechanical interlock shown in these linear-elastic analyses may be expected for the structural adhesive examined in this study. Similarly, [4] found that introducing a bolt at the centre of a hybrid, bonded/bolted joint had limited effect on the magnitude of the stresses at the ends of the overlap and that the adhesive transferred approximately 98% of the applied load as a result of the small relative displacement which occurs between the adherends of the adhesive joint. A more ductile adhesive may allow for greater influence from the mechanical interlock prior to damage initiation. In joint C, the maximum normal stress was present at the profile face on the female end of the profile and was 33.9% greater than the maximum normal stress of the baseline. The lesser tensile stress present on the profile face of joint N was a result of the greater profile face area and the less significant loose fit condition observed. Further differences between joints C and N follow from the variation in the interlocking profile length, depth, and width; resulting in different deformation in the vicinity of the profile for each configuration.

4.2.1. Load Path Investigation

In order to provide a better understanding of the mechanisms of load transfer in the interlocking joints, a novel visualisation technique developed by Kelly and Elsley [37] was employed. This technique employs *load paths*, which may be defined as the trajectory taken by a unit of applied load in a prescribed direction through a structure; beginning at a point of application and ending at an equilibrating reaction. These trajectories can be established through a series of total stress "pointing" vectors produced from the columns of the stress tensor, $\boldsymbol{\sigma}$, at each node where it is known. A pointing vector for stress in the x direction may be derived from Eq. 8. Computing this equation at each node in the finite element mesh produces a vector field, giving the trajectories of the load path vector, $\boldsymbol{V^x}$ that defines load flow in the x direction. In the present work, a two-step, second-order

Runge-Kutta algorithm [38] was subsequently used to generate load path contours, tangent to the load path vectors, identifying paths along which the x component of load remains constant, defining the load path. If these paths are equally spaced and originate in a section carrying uniform stress, they may be considered as contours between which an equal amount of force is transferred. Thus, paths which are closer together illustrate the presence of a stress concentration. Similar equations to Eq. 8 may be produced to indicate the trajectories of force in the y & z directions, although only the x direction is considered herein.

$$\boldsymbol{V^x} = \sigma_{xx}\boldsymbol{i} + \sigma_{yx}\boldsymbol{j} + \sigma_{zx}\boldsymbol{k} \tag{8}$$

where $\boldsymbol{V^x}$ is the load path vector, defining load flow in the x direction, σ_{xx}, σ_{yx} & σ_{zx} are components of the stress tensor, $\boldsymbol{\sigma}$, and $\boldsymbol{i}$, $\boldsymbol{j}$ & $\boldsymbol{k}$ are unit vectors in the x, y & z directions respectively.

This analysis was based on the linear-elastic joint models, in order to determine the load distribution in the joints prior to damage initiation. Joint N was investigated and compared to the baseline joint. The resulting load-paths are presented in Figure 9. These plots indicate the trajectories of the x component of force through the joint overlap overlaid on contours of the direct stress in the loading direction, σ_{xx}. The load-path analysis directly supports the findings of the adhesive stress analysis presented in Section 4.2. In both configurations, the majority of load was transferred through the adherends close to the bond plane of the joint, parallel with the applied force. In the baseline joint, load was predominantly transmitted through the ends of the joint overlap, as it is clear that load paths concentrate in these regions. At the constrained end of each adherend the load-paths run horizontally, in line with the applied force; as such, shear loading of the adhesive is dominant. Towards the end of each adherend the load paths move away from the bond plane and become more vertical, corresponding to the bending moment existing on the SLJ. This was indicative of the strong tensile normal stresses on the adhesive at the ends of the joint overlap. The superimposed contours of σ_{xx} indicate that tensile elongation of the adherends is greatest at the constrained ends of the adherends and reduces approaching the free ends, signifying a non-uniform tangential stress distribution in correspondence with Volkersen's [35] concept of differential shear.

The distribution of load-paths in the interlocking joint was much less uniform, particularly in the female adherend as the interlocking geometry impeded their course. Similarly, the majority of load was transferred through the ends of the joint overlap. However, at the centre of the overlap, a portion of load was transferred directly across the adhesive layer into the male profile. These load paths are indicative of the strong tensile normal stress acting on the adhesive at this profile face, as in Figure 8.

The majority of load which was carried through this region propagated into the male adherend, past point (i), and towards its constrained end. The paths clustered together at point (i) representing a stress concentration. A lesser portion of load was transferred through the profile, about point (ii), and back into the female adherend. This explains the tensile normal stress acting on the adhesive at this profile face, as per Figure 8, as well as the lack of mechanical contact from the interlock. These load-paths also changed direction as they passed through the adhesive layer, indicative of the shear dominated loading of the adhesive which was caused by bending of the joint.

It was clear that minimal load passed through the base of the interlocking profile, corresponding to Figure 8. There were also no load-paths in the vicinity of points (iii) and (iv) in both the baseline and interlocking joints as bending is predominant. As such no force was transferred in the x-direction through these regions between the constrained ends of the joint.

4.3. Progressive Damage & Failure

Cohesive fracture in a standard, adhesively bonded SLJ initiates at the free ends of the overlap area and propagates rapidly across the bond area, resulting in sudden, catastrophic failure. In contrast, the interlocking adhesive joints investigated herein have demonstrated much more progressive failure, as shown in Figures 5. This progressive type of failure is brought about as fracture must develop around the interlocking profile and may be characterised in six stages. To illustrate this, the load-displacement curve, in Figure 10, will be discussed in combination with von Mises stress contours in a cross-section of the joint overlap at the x-y mid-plane and a plan view of the cohesive element layer depicting damage evolution and the propagation of fracture, in Figure 11. Joint N is discussed herein although this behaviour is similarly apparent for various interlocking joint configurations.

The initial response of the interlocking joint was linear, very similar to that of the baseline joint, with minimal difference in stiffness. Stress concentrated at the ends of the joint overlap as demonstrated previously in Figures 8 and 9. Prior to point 1, damage initiated in the cohesive elements at the free ends of the bond area. Beyond this point, damage developed in the adhesive layer from the overlap ends and the influence of the interlocking geometry on the mechanical response became more apparent.

As a consequence of the asymmetric stress distribution prior to damage initiation, discussed in Section 4.2, damage initially evolved further from the female end of the bond than the male end. At point 2, the joint achieved its ultimate failure load as damage propagated through the adhesive from female end of the bond and reached the face of the interlocking profile, where significant tensile normal stresses were previously highlighted (Figure 8). Consequentially, fracture initiated at the female end of

the bond and began to propagate rapidly towards the face of the profile. This explains why increasing profile length has a negative effect on ultimate failure load (Figure 6a); i.e. for a longer profile, damage must propagate a shorter distance to reach the face of the profile, thus fracture occurs at a lower load.

The joint experienced an immediate drop in load as fracture occurred at point 2 and began to develop around the interlocking profile at point 3. The male end of the bond interestingly remained intact at this stage due to the asymmetric elastic stress distribution outlined previously (Figure 8). There was a slight increase in load preceding point 4; upon which, all of the cohesive elements at the female end of the interlocking profile had failed. As a result, fracture initiated at the male end of the bond and subsequently propagated simultaneously from the male and female ends of the joint overlap, and around the interlocking profile. The load endured by the joint decreased prior to point 5. At this stage fracture had propagated across the majority of the bond with the exception of a small area around the profile face at the male end of the bond.

The load on the joint increased once again between points 5 and 6. At this stage, compressive forces were induced on the remaining adhesive by the interlocking morphology. This arrested fracture from propagating across the profile face at the male end of the joint, prolonging failure of the joint. Substantial plastic deformation followed, occurring in the female adherend and locally at the base of the profile in the male adherend. At point 6, the joint ultimately failed as the profile sheared out of its interlocked position and ceased to carry load.

Haghpanah et al. [14] experimentally tested an alternative adhesively bonded interlocking joint concept and observed that initial failure, in the adhesive, resulted in a drop in the associated load-displacement curve but not the complete loss of load bearing capacity of the joint. It was shown that morphological details of the adherends could impede a crack from propagating along the bond. Once the crack was arrested, the joint sustained further loading which induced plastic deformation of the adherends, resulting significant improvements of the joint's work to failure. It is apparent that the mechanism governing these improvements is the same as that identified for the interlocking adhesive joints presented herein; which is testament to the validity of these numerical results.

In general, the progressive fracture behaviour demonstrated by the interlocking joints results in far greater displacement at failure compared to the baseline case, resulting in much greater work to failure. This is a significant development as the drop in load experienced by the interlocking joint during initial failure provides an opportunity for the detection of serious damage prior to catastrophic failure of the joint and complete loss of load bearing capacity. This type of response was most apparent in joints

with high values for each of profile depth, width and angle. The most significant improvements in work to failure were achieved for joints which displayed considerable reloading between points 5 and 6 (in Figure 10), this was only achieved for joints with the highest values of profile depth, width and angle, for joints which sustained substantial plastic deformation. This also explains why profile width (X_3) and angle (X_4) showed considerable positive quadratic effects.

In the case of joint N, before achieving cohesive failure, a stress concentration at the root of the profile in the male adherend reached the ultimate tensile strength of the material [18]. This corresponds approximately to the stress concentration identified in the load path analysis, in Figure 9, (i). This occurrence was defined as adherend failure and thus, failure of the joint, as indicated in Figure 10. As such, the total improvement in work to failure for joint N was calculated from this point. This is a conservative assumption given that the initiation and evolution of damage in the metallic adherend would absorb considerable energy prior to catastrophic failure of the adherend; which may not even occur before cohesive failure of the joint. It is important to note that improvements in work to failure of up to 63.5%, were also achieved for joints which failed cohesively prior to reaching the ultimate tensile strength in the adherend.

4.4. Alternative Adhesive Properties

In order to demonstrate the versatility of the interlocking adhesive joint concept and the optimum configuration presented herein, two alternative adhesive systems were selected. The structural adhesives, from Nagase ChemteX, were XNR6823 and XNR6852. As a result of their contrasting mechanical properties, the former is identified as brittle and the latter as ductile. The CZDM properties of these adhesive systems were published by Ribeiro et al. [39] and those applied herein are outlined per Table 5. In order to assess the applicability of each to the present concept, interlocking joint N was simulated and compared to a baseline, standard adhesively bonded joint modelled with equivalent properties. The mechanical response of these joints is presented per Figure 12.

The propagation of fracture in the joint with the brittle adhesive (XNR6823) occurred similarly to that determined for the primary adhesive system, Hysol 9466 (Figure 10), resulting in similar features which were apparent in the mechanical response. The ultimate failure load of the of the interlocking joint was slightly lower than the baseline but there was a considerable improvement in the work to failure. In contrast to this, the ductile adhesive (XNR6852) allows for greater relative displacement between the male and female adherends. Accordingly, the interlocking geometry has greater influence on the mechanical response of the joint prior to the propagation of fracture. As a result, the interlocking

joint presents an improvement in ultimate failure load compared to the baseline. The interlocking joint with the ductile adhesive also exhibits progressive development of fracture as it propagates around the interlocking profile, resulting in significant improvement of the joint's work to failure.

5. Conclusion

The influence of interlocking bond-surface morphology on the mechanical response of adhesively bonded joints was investigated using finite element analysis and the design of the interlocking geometry was optimised through an adaptive surrogate modelling design optimisation procedure. The sensitivity of the interlocking profile design factors were investigated based on the resulting surrogate model. It has been shown that the interlocking profile length has the most significant *linear main* effect on the ultimate failure load, profile length should be minimised to maximise ultimate failure load; while profiles with length less than approximately 50% of the bond length (x-direction) produced a reduction in ultimate failure load of less than 5% compared to the baseline. Profile depth and width also have significant synergistic interactions with profile length. Profile angle was determined to have negligible influence on ultimate failure load. In contrast, the synergistic interaction between profile width and angle had the most significant positive effect on the joint's work to failure while also demonstrating highly non-linear response. It was necessary to adopt high values of profile depth, width, and angle to achieve the most significant improvements in work to failure. Profile length had a minimal effect on the joint's work to failure.

Linear-elastic FE models of the concept show that the incorporation of interlocking surfaces results in an asymmetric tangential stress distribution in the adhesive layer, with reduced average stress compared to a standard adhesive joint. The distribution of normal stress is more similar to a standard joint, although concentrations in tensile normal stress were observed on the faces of the interlocking profile. FE models incorporating damage in the adhesive layer showed that failure of the joint remained a function of the stress state at the free ends of the joint overlap where fracture initiated. However, significant improvements in work to failure were achieved as a result of the more progressive failure process exhibited by the interlocking joints. Improvements in ultimate failure load were less significant for the interlocking adhesive joint when combined with a relatively brittle structural adhesive, although optimal joints demonstrated minimal effect to working load limit compared to a standard adhesive joint. The chosen optimum interlocking joint presented an improvement in work to failure of 86.5% with a reduction in ultimate failure load of only 1.2% compared to a traditional adhesively bonded

joint modelled with equivalent properties.

In order to demonstrate the adaptability of the interlocking adhesive joint concept and the optimum configuration presented herein, two alternative adhesive systems were selected; representing a relatively brittle and a ductile structural adhesive. It was observed that the application of the ductile adhesive allows for greater influence of the interlocking geometry prior to the initiation of fracture, resulting in significant improvement of the joint's ultimate failure load. Further investigation of the interlocking adhesive joint concept in combination with ductile structural adhesives will be the subject of future work. In addition, experimental tests should yield further improvements in work to failure as it would be possible to consider the full response of the interlocking joint. These tests may also provide further insight into the joint's failure mechanisms and determine whether it is necessary to include more sophisticated damage models in future investigations.

Acknowledgements

The authors acknowledge the financial support of Science Foundation Ireland under Grant No. 13/IA/1833 and the Irish Research Council (IRC) for funding under their Government of Ireland Postgraduate Scheme through Grant No. GOIPG/2014/945. The authors also wish to acknowledge the DJEI/DES/SFI/HEA Irish Centre for High-End Computing (ICHEC) for the provision of computational facilities and support.

References

[1] J. Tomblin, K. Strole, G. Dodosh, L. Ilcewicz, Assessment of industry practices for aircraft bonded joints and structures DOT/FAA/AR-05/13, Tech. rep., Office of Aviation Research, Washington D.C. 20591 (2005).

[2] M. D. Banea, L. F. M. da Silva, Adhesively bonded joints in composite materials: an overview, Proceedings of the Institution of Mechanical Engineers Part L: Journal of Materials-Design and Applications 223 (1) (2009) 1–18.

[3] G. Kelly, Quasi-static strength and fatigue life of hybrid (bonded/bolted) composite single-lap joints, Composite Structures 72 (1) (2006) 119–129.

[4] G. Kelly, Load transfer in hybrid (bonded/bolted) composite single-lap joints, Composite Structures 69 (1) (2005) 35–43.

[5] R. D. S. G. Campilho, A. M. G. Pinto, M. D. Banea, L. F. M. Da Silva, Optimization study of hybrid spot-welded/bonded single-lap joints, International Journal of Adhesion and Adhesives 37 (2012) 86–95.

[6] F. Moroni, A. Pirondi, F. Kleiner, Experimental analysis and comparison of the strength of simple and hybrid structural joints, International Journal of Adhesion and Adhesives 30 (5) (2010) 367–379.

[7] L. F. M. da Silva, A. Pirondi, A. Öchsner (Eds.), Hybrid adhesive joints, 1st Edition, Vol. 6, Springer Science & Business Media, Berlin Heidelberg, 2011.

[8] S. M. Darwish, A. Al-Samhan, Design rationale of weld-bonded joints, International Journal of Adhesion and Adhesives 24 (5) (2004) 367–377.

[9] T. Sadowski, M. Kneć, P. Golewski, Spot WeldingâĂŞAdhesive Joints: Modelling and Testing, The Journal of Adhesion 90 (4) (2014) 346–364.

[10] M. Fu, P. K. Mallick, Fatigue of hybrid (adhesive/bolted) joints in SRIM composites, International Journal of Adhesion and Adhesives 21 (2) (2001) 145–149.

[11] F. Smith, COMELD - An innovation in composite to metal joining, in: Composites Processing 2004, CPA, Bromsgrove, UK, 2004.

[12] T. P. Lang, P. K. Mallick, Effect of recessing on the stresses in adhesively bonded single-lap joints, International Journal of Adhesion and Adhesives 19 (4) (1999) 257–271.

[13] Q.-G. Zeng, C. T. Sun, Novel Design of a Bonded Lap Joint, AIAA Journal 39 (10) (2001) 1991–1996.

[14] B. Haghpanah, S. Chiu, A. Vaziri, Adhesively bonded lap joints with extreme interface geometry, International Journal of Adhesion and Adhesives 48 (2014) 130–138.

[15] D. J. O'Dwyer, N. P. O'Dowd, C. T. McCarthy, In-situ SEM mechanical testing of miniature bonded joints, International Journal of Adhesion and Adhesives 50 (2014) 57–64.

[16] Simulia® - Abaqus®, User's Manual, Version 6.14, Tech. rep., Hibbitt, Karlsson & Sorensen, Inc., Pawtucket, USA (2014).

[17] Aalco Metals Ltd., Aluminium alloy 5754 - H111 treadplate: material data sheet, Tech. rep., aalco, Surrey (2015).

[18] F. Ozturk, S. Toros, H. Pekel, Evaluation of tensile behaviour of 5754 aluminium-magnesium alloy at cold and warm temperatures, Materials Science and Technology 25 (7) (2009) 919–924.

[19] J. H. Hollomon, Tensile deformation, AIME Trans 12 (4) (1945) 1–22.

[20] Loctite Hysol 9466, Technical Data Sheet, Tech. rep. (2014).

[21] L. Goglio, L. Peroni, M. Peroni, M. Rossetto, High strain-rate compression and tension behaviour of an epoxy bi-component adhesive, International Journal of Adhesion and Adhesives 28 (7) (2008) 329–339.

[22] T. Andersson, U. Stigh, The stress-elongation relation for an adhesive layer loaded in peel using equilibrium of energetic forces, International Journal of Solids and Structures 41 (2004) 413–434.

[23] K. Leffler, K. S. Alfredsson, U. Stigh, Shear behaviour of adhesive layers, International Journal of Solids and Structures 44 (2) (2007) 530–545.

[24] J. L. Högberg, Mixed mode cohesive law, International Journal of Fracture 141 (3-4) (2006) 549–559.

[25] A. Pirondi, D. Fersini, E. Perotti, F. Moroni, Applicability of cohesive zone model in fracture simulation for several geometries of bonded joints, in: IGF19, Milano, 2007.

[26] M. De Moura, J. Gonçalves, J. Chousal, R. Campilho, Cohesive and continuum mixed-mode damage models applied to the simulation of the mechanical behaviour of bonded joints, International Journal of Adhesion and Adhesives 28 (8) (2008) 419–426.

[27] D. Castagnetti, E. Dragoni, A. Spaggiari, Failure analysis of complex bonded structures: Experimental tests and efficient finite element modelling by tied mesh method, International Journal of Adhesion and Adhesives 31 (5) (2011) 338–346.

[28] G. G. Wang, S. Shan, Review of Metamodeling Techniques in Support of Engineering Design Optimization, Journal of Mechanical Design 129 (4) (2007) 370–380.

[29] A. I. J. Forrester, A. Sóbester, A. J. Keane, Engineering Design via Surrogate Modelling: A Practical Guide, 1st Edition, Wiley, West Sussex, UK, 2008.

[30] D. R. Jones, A Taxonomy of Global Optimization Methods Based on Response Surfaces, Journal of Global Optimization 21 (2001) 345–383.

[31] K. Deb, A. Pratap, S. Agarwal, T. Meyarivan, A fast and elitist multiobjective genetic algorithm: NSGA-II, IEEE Transactions on Evolutionary Computation 6 (2) (2002) 182–197.

[32] Q. Yang, B. Cox, Cohesive models for damage evolution in laminated composites, International Journal of Fracture 133 (2) (2005) 107–137.

[33] A. Turon, C. Dávila, P. Camanho, J. Costa, An engineering solution for mesh size effects in the simulation of delamination using cohesive zone models, Engineering Fracture Mechanics 74 (10) (2007) 1665–1682.

[34] T. Simpson, J. Poplinski, P. N. Koch, J. Allen, Metamodels for Computer-based Engineering Design: Survey and recommendations, Engineering With Computers 17 (2) (2001) 129–150.

[35] O. Volkersen, Die Nietkraftverteilung in zugbeanspruchten Nietverbindungen mit konstanten Laschenquerschnitten, Luftfahrtforschung 15 (1/2) (1938) 41–47.

[36] M. Goland, E. Reissner, The stresses in cemented joints, Journal of applied mechanics 11 (1) (1944) A17–A27.

[37] D. Kelly, C. Reidsema, A. Bassandeh, G. Pearce, M. Lee, On interpreting load paths and identifying a load bearing topology from finite element analysis, Finite Elements in Analysis and Design 47 (8) (2011) 867–876.

[38] Tecplot Inc., User's Manual, Version 10, Tech. rep., Tecplot, Inc., Bellevue, Washington (2004).

[39] T. E. A. Ribeiro, R. D. S. G. Campilho, L. F. M. da Silva, L. Goglio, Damage analysis of composite-aluminium adhesively-bonded single-lap joints, Composite Structures 136 (2016) 25–33.

Tables

Table 1: Mechanical properties of the aluminium alloy, AA5754 [17, 18].

E	ν	σ_y	K	n	σ_{uts}
68 GPa	0.33	111.46 MPa	496.4 MPa	0.31	299.58 MPa

Table 2: Mechanical [20] and cohesive zone model [25] properties of the adhesive, Hysol 9466.

E	ν	$\sigma_{uts_{tensile}}$	k	t^o	G^C
1.718 GPa	0.35	32 MPa	31.24 GPa	60 MPa	690 J/m^2

Table 3: Side constraints imposed on interlocking profile design factors.

$Factor$	$LowerBound$	$UpperBound$
X_1	0.7 mm	4.5 mm
X_2	0.05 mm	1.0 mm
X_3	0.7 mm	6.5 mm
X_4	35.0°	88.0°

Table 4: Excerpt of pertinent input and output data from the ASMDO process.

$Joint$	$X_1[mm]$	$X_2[mm]$	$X_3[mm]$	$X_4[°]$	$y_1[N]$	$y_2[mJ]$
A	1.12	0.15	1.34	46.7	1156.4	133.1
B	1.95	1.0	5.86	70.5	1124.0	170.4
C	3.21	0.76	4.7	85.4	991.8	158.3
D	1.65	0.76	1.51	86.4	1153.0	128.8
E	4.42	0.8	3.63	87.5	855.0	186.3
F	1.35	0.74	4.76	85.4	1149.6	165.0
G	1.42	0.22	3.43	72.1	1155.8	131.0
H	1.92	0.13	4.88	81.1	1156.4	132.1
I	1.19	0.6	4.7	87.5	1152.6	157.4
J	1.12	0.15	1.16	88.0	1156.3	133.0
K	1.12	0.15	5.05	88.0	1155.7	133.6
L	1.19	1.0	6.33	88.0	1146.4	236.6
M	1.16	1.0	5.28	88.0	1148.4	185.8
N	1.5	0.91	5.63	85.9	1141.2	259.6

Table 5: Cohesive zone model properties of the brittle and ductile structural adhesives, XNR6823 and XNR6852 respectively [39].

$Property$	$XNR6823$	$XNR6852$
k $[GPa]$	47.2	40.6
t_n^o $[MPa]$	57	48
t_s^o $[MPa]$	32.9	20.5
G_n^C $[J/m^2]$	1180	2000
G_s^C $[J/m^2]$	1500	4400

Figures

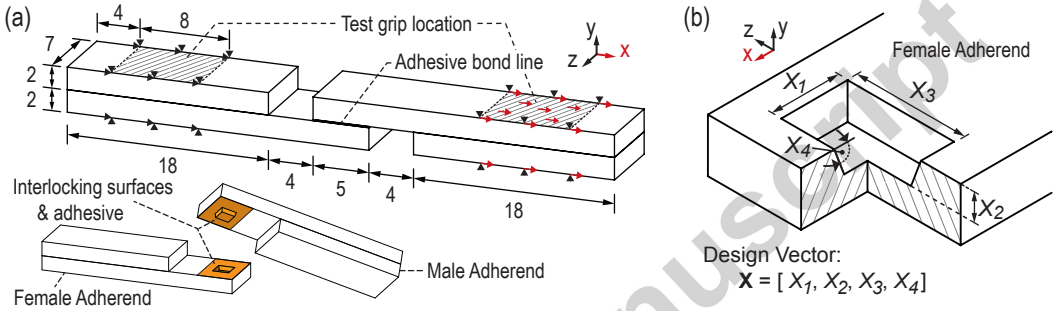

Figure 1: Miniature SLJ (a) geometry and boundary conditions, with dimensions in millimetres and (b) truncated, square pyramid interlocking profile geometry and corresponding geometric factors.

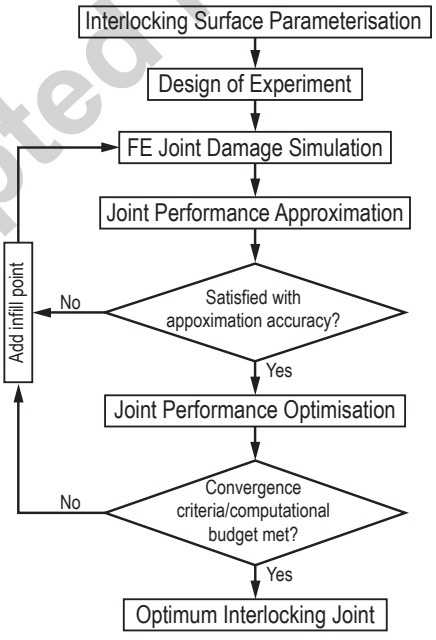

Figure 2: Adaptive surrogate modelling design optimisation process applied to interlocking adhesive joints.

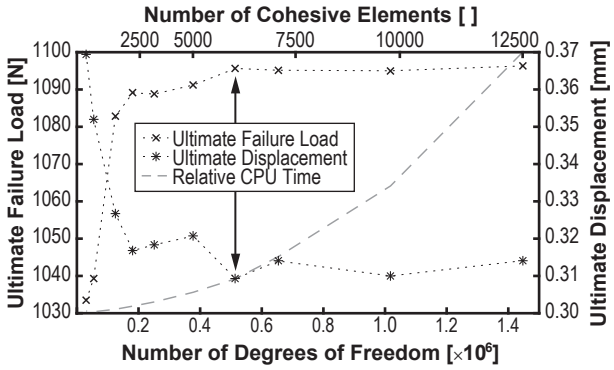

Figure 3: Mesh independence study, outlining the ultimate failure load and the ultimate displacement for an interlocking joint model with various degrees of discretisation.

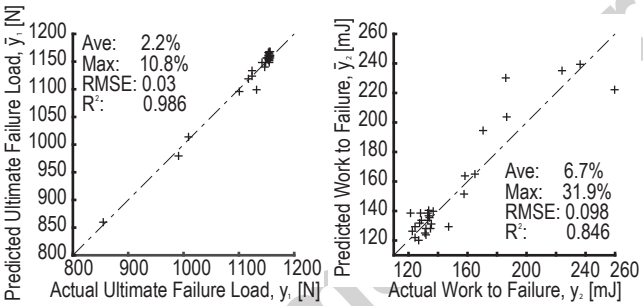

Figure 4: Surrogate model error predictions for the ultimate failure load (left) and work to failure (right).

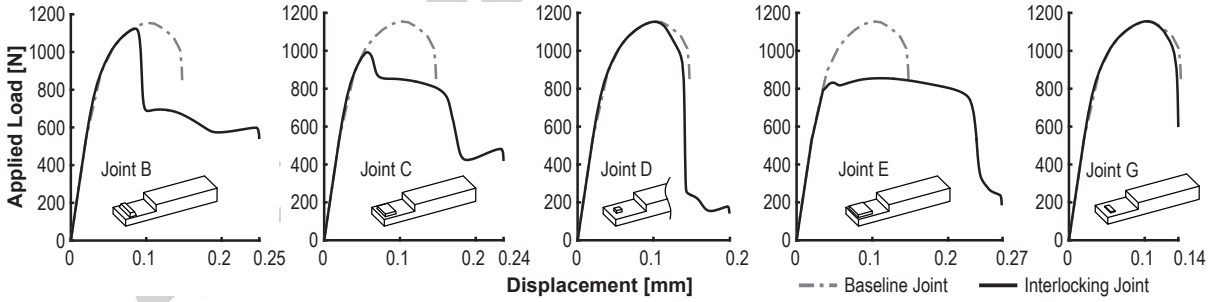

Figure 5: Load-displacement response of various interlocking joints compared to that of a baseline, standard adhesively bonded joint modelled with equivalent properties; inset is the male adherend of each joint.

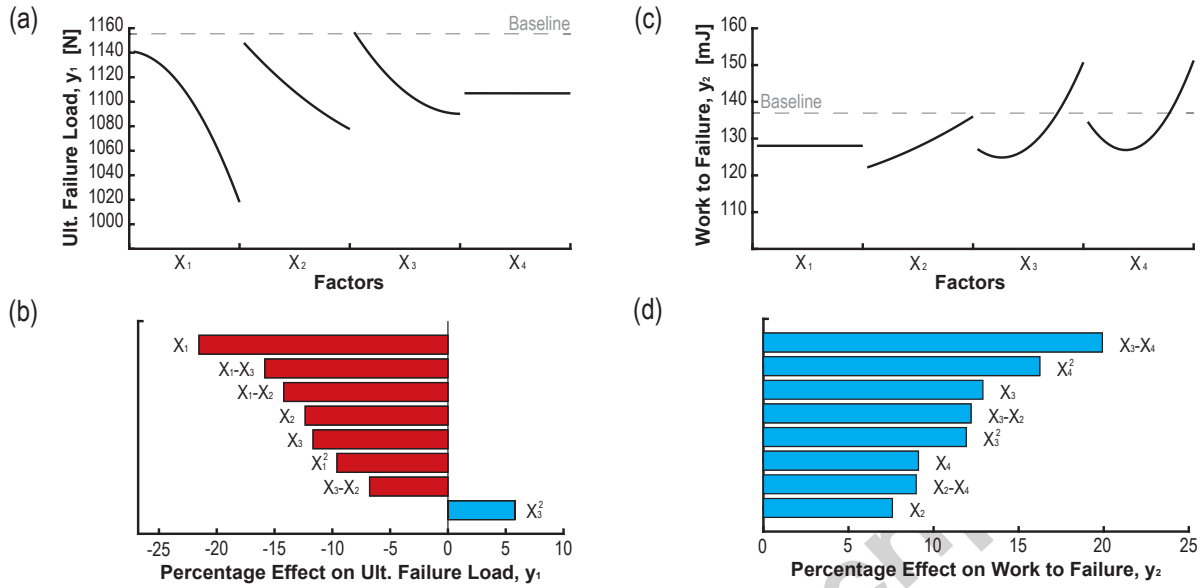

Figure 6: Estimated factor effects of each response: (a) and (b) correspond to ultimate failure load, and (c) and (d) to work to failure; main effects plots are shown on top, and Pareto charts showing magnitude of linear-main, quadratic, and interaction effects relative to one another on bottom.

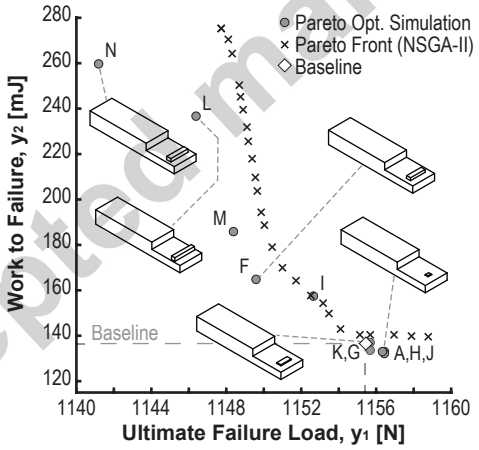

Figure 7: Pareto plot, comparing Pareto optimal simulations, including the selected optimum, N, to the Pareto frontier identified by the optimisation algorithm based on the surrogate model.

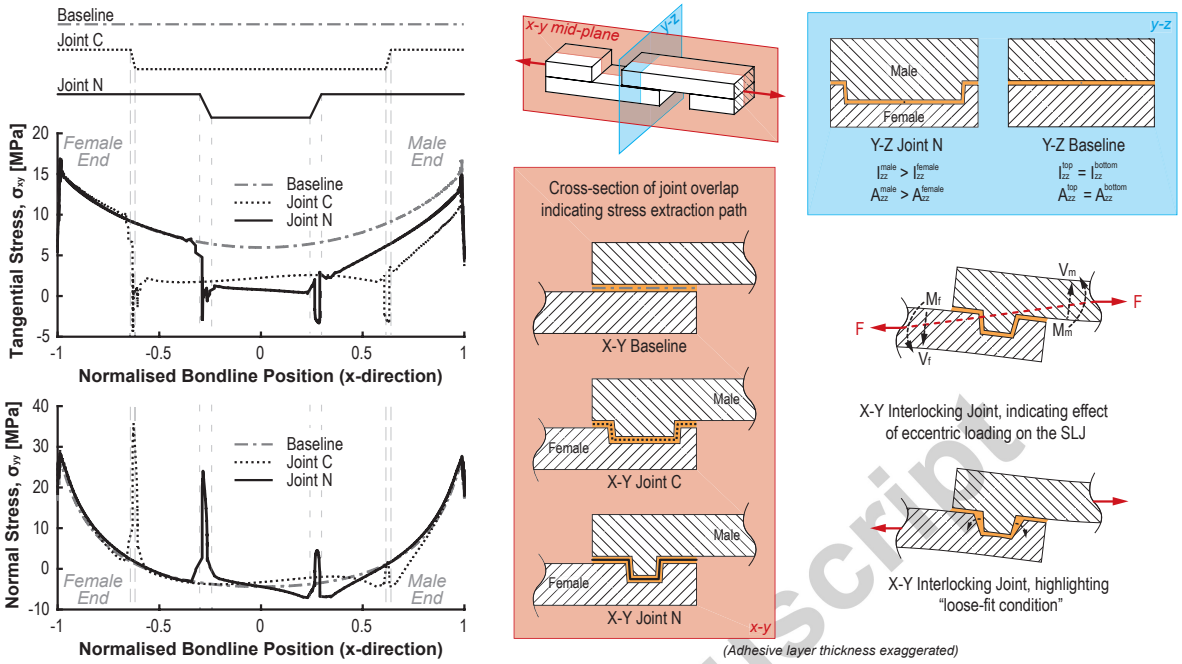

Figure 8: Distribution of tangential (top) and normal (bottom) stress along the x-y mid-plane of the adhesive layer for interlocking joints C and N, compared to the baseline (left) and schematic drawings of the joint overlap region used to explain the differences in the stress distribution of the interlocking joints (right).

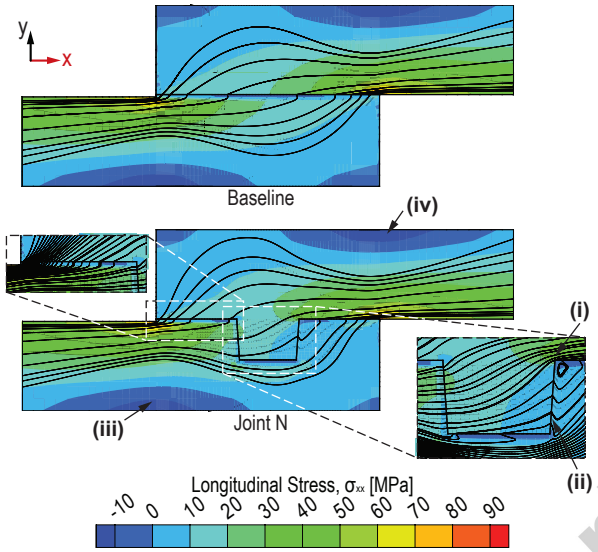

Figure 9: Cross-sectional view at the x-y mid-plane of the joint overlap with the trajectories of load-paths indicating load flow in the x direction, overlaid on contours of σ_{xx}.

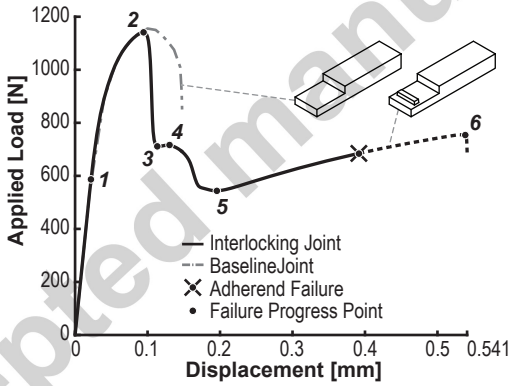

Figure 10: Load-displacement response of joint N, outlining the stages of progressive failure.

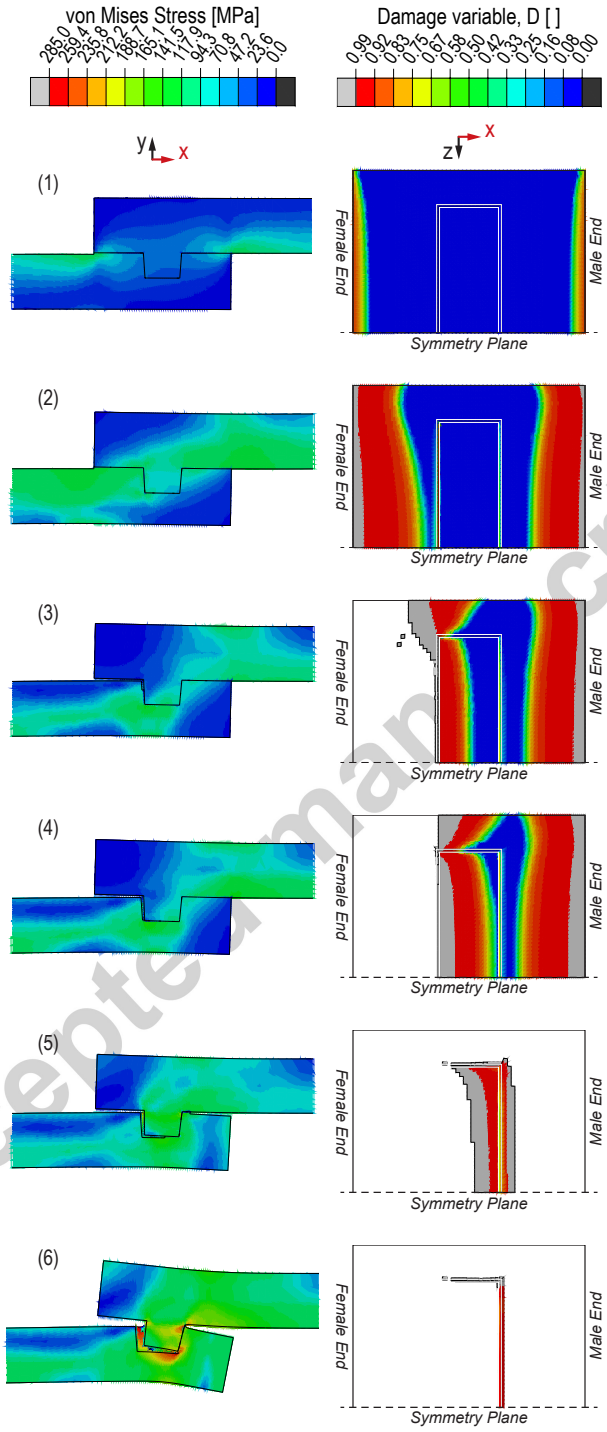

Figure 11: Analysis of progressive failure for joint N; showing von Mises stress contours in a cross-section of the joint overlap at the x-y mid-plane (left) and a plan view of the cohesive element layer depicting element damage (right), during various stages of loading, corresponding to Figure 10.

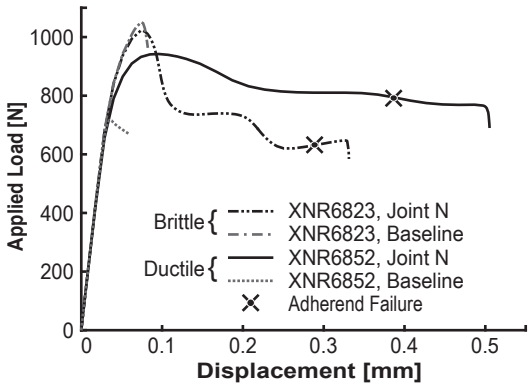

Figure 12: Mechanical response of interlocking joint N compared to a baseline joint for each of a brittle and a ductile structural adhesive.